AGU PUBLICATIONS

JGR

Journal of Geophysical Research: Oceans

RESEARCH ARTICLE

10.1002/2014JC009839

Key Point:
- Breaking waves enhance flows into an ocean inlet

Correspondence to:
A. Wargula,
awargula@whoi.edu

Citation:
Wargula, A., B. Raubenheimer, and S. Elgar (2014), Wave-driven along-channel subtidal flows in a well-mixed ocean inlet, *J. Geophys. Res. Oceans*, *119*, 2987–3001, doi:10.1002/2014JC009839.

Received 21 JAN 2014
Accepted 14 APR 2014
Accepted article online 17 APR 2014
Published online 20 MAY 2014

Wave-driven along-channel subtidal flows in a well-mixed ocean inlet

Anna Wargula[1], Britt Raubenheimer[1], and Steve Elgar[1]

[1]Woods Hole Oceanographic Institution, Woods Hole, Massachusetts, USA

Abstract Observations of waves, flows, and water levels collected for a month in and near a long, narrow, shallow (∼ 3000 m long, 1000 m wide, and 5 m deep), well-mixed ocean inlet are used to evaluate the subtidal (periods > 30 h) along-inlet momentum balance. Maximum tidal flows in the inlet were about 1.5 m/s and offshore significant wave heights ranged from about 0.5 to 2.5 m. The dominant terms in the local (across the km-wide ebb shoal) along-inlet momentum balance are the along-inlet pressure gradient, the bottom stress, and the wave radiation-stress gradient. Estimated nonlinear advective acceleration terms roughly balance in the channel. Onshore radiation-stress gradients owing to breaking waves enhance the flood flows into the inlet, especially during storms.

1. Introduction

The hydrodynamics of well-mixed tidal inlets, which are transitional regions between bays and the open ocean, have been studied for many years. Numerical simulations suggest that the dominant momentum balance terms governing tidal circulation at well-mixed, shallow tidal inlets depend on the tidal phase [*Hench and Luettich*, 2003]. During maximum ebb or flood, the streamwise tidal balance in the straits of a long, narrow inlet is predicted to be between the pressure gradient and bottom stress [*Hench et al*., 2002, idealized inlet II]. Local advective accelerations may become important offshore of the straits during peak flows, and in the straits near slack tide. In natural inlets, the local momentum balance may be affected by bathymetric variations [*Blanton et al*., 2002; *Hench and Luettich*, 2003; *Buijsman and Ridderinkhof*, 2007]. For example, the bed stress becomes increasingly important with decreasing depth (e.g., on the shoals and in shallow inlets) and near headlands [*Signell and Geyer*, 1991; *Friedrichs and Madsen*, 1992; *Buijsman and Ridderinkhof*, 2007]. In addition, exchange between the different openings of multiple inlet systems may alter the hydrodynamic behavior of each inlet [*Boon and Byrne*, 1981; *Speer and Aubrey*, 1985; *Aubrey et al*., 1993; *Chant*, 2001; *Salles*, 2001; *Salles et al*., 2005; *Pacheco et al*., 2010].

Subtidal fluctuations also can have a significant effect on the fluxes through inlets and on the momentum balances [*Swenson and Chuang*, 1983]. For example, strong winds can cause pressure gradients that change the direction or strength of the inlet flows [*Smith*, 1993; *Geyer*, 1997; *Wong and Moses-Hall*, 1998; *Chant*, 2001; *Wong and Valle-Levinson*, 2002; *Cáceres et al*., 2003; *Waterhouse and Valle-Levinson*, 2010; *Tutak and Sheng*, 2011; *Li*, 2013]. Numerical simulations also suggest that wave forcing may be important along ocean coasts [*Piedracoba et al*., 2005; *Bertin et al*., 2009; *Malhadas et al*., 2009; *Olabarrieta et al*., 2011; *Dodet et al*., 2013]. However, there are few field-based studies of wave effects on inlet flows.

Along the shoreline on either side of the inlet, cross-shore decreases in the wave momentum flux (radiation stress) owing to wave breaking are balanced by increases in the mean sea level (setup) [*Longuet-Higgins and Stewart*, 1964; *Raubenheimer et al*., 2001; *Apotsos et al*., 2007; *Apotsos et al*., 2008, and references therein]. Near an inlet, model simulations suggest cross-shore radiation-stress gradients owing to wave dissipation across the ebb shoal can drive fluxes into the inlet [*Bertin et al*. 2009; *Malhadas et al*., 2009], which may result in increased bay water levels [*Olabarrieta et al*., 2011; *Dodet et al*., 2013]. If the shoals are asymmetric and waves break primarily on one side of an inlet connected to an enclosed bay, flows into the inlet driven by the wave breaking may be balanced by a return flow on the opposite side of the inlet [*Piedracoba et al*., 2005]. In addition, wave-forced flows may constrict the ebb current jet, causing it to narrow and intensify in the main inlet channel. Wave-induced currents near the ebb shoal may be as large as 1 m/s [*Dodet et al*., 2013]. If a steady state is not reached or if water is not confined to the bay (e.g., owing to multiple inlets), the onshore radiation-stress gradients may result in onshore-directed mass flux through the inlet,

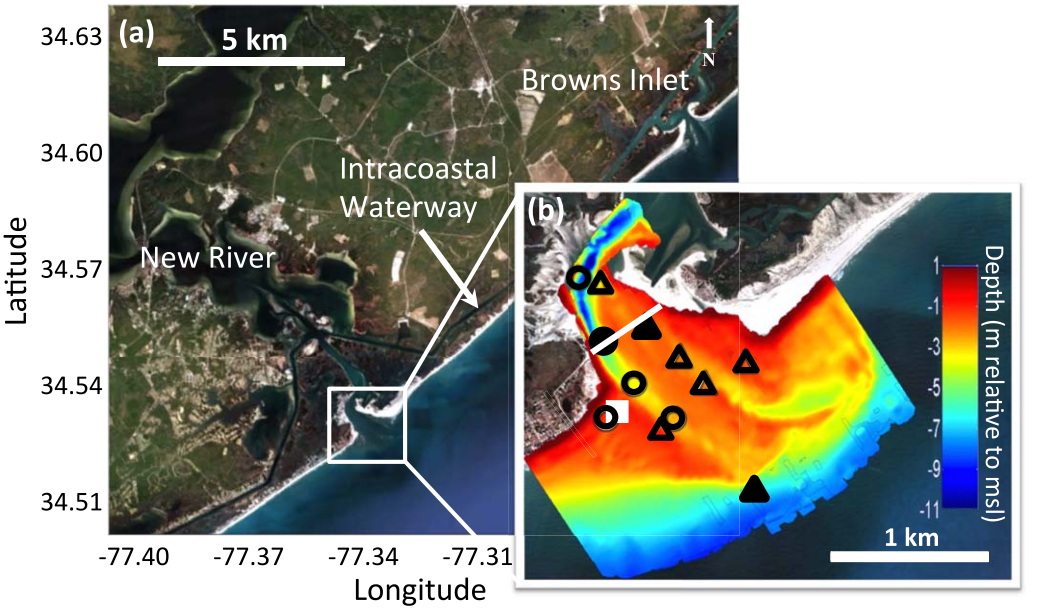

Figure 1. (a) Google Earth image of the North Carolina coast (latitude and longitude indicated on axes) showing New River, the Intracoastal Waterway, and Browns Inlet and (b) close-up view of New River Inlet (square white outline in Figure 1a) with instrument locations (black circles and triangles are current profilers and current meters, respectively) and bathymetry (color contours, scale on the right, red is shallow, blue is deeper water) superposed. The filled black circle and triangles ("offshore" of the ebb shoal, in the inlet "channel," and on the inlet "shoals") are used for along-inlet balances. Open black circles and triangles are sites of other measurements. The white line between the channel and the shoals sites is a cross-inlet transect surveyed with a boat-mounted current profiler (see Appendices A and B). The white square is the location of onsite wind measurements.

and may be balanced by a combination of friction of the onshore-directed current, an offshore-directed pressure gradient, and advective acceleration [*Bertin et al.*, 2009; *Malhadas et al.*, 2009; *Olabarrieta et al.*, 2011].

Here in situ measurements of water levels, currents, and waves at a well-mixed tidal inlet in a system connected to other inlets up and down the coast are used to show that breaking-wave driven along-inlet (cross shore) radiation-stress gradients significantly affect subtidal flows in the inlet mouth.

2. Field Measurements

2.1. Site Location

New River Inlet is roughly 100 km south of Cape Hatteras, on the coast of North Carolina (Figure 1) [*Riggs et al.*, 1995]. The inlet width is about 1000 m at the entrance and tapers to 100 m about 1000 m upstream after two sharp 90° bends. New River extends about 25 km upstream from the inlet, and the backbay has an area of about 68 km^2 [*MacMahan et al.*, 2014]. About 3 km upstream from its mouth, the inlet intersects the Intracoastal Waterway (ICW) (Figure 1a). The ICW continues north and south from New River, connecting to many additional inlets, including Browns Inlet 12 km to the north (Figure 1) and New Topsail Inlet 36 km to the south (not shown). Freshwater discharge is minimal, and the water is well mixed in the region seaward of the intersection with the ICW. In late April 2012, salinities measured in the ocean, inlet mouth, and near the ICW intersection were about 36 psu.

The bathymetry was surveyed (relative to NAVD88) five times (16–17 April; 1–2, 10–11, 17–18, and 25 May) during the 2012 field program. Overall temporal changes in the sand levels on the ebb shoal and in the inlet mouth typically were less than about 0.3 m, and the results here are not sensitive to which bathymetry is used (elevation changes at the sensors used in the momentum balance analysis were less than 0.1 m). Thus, bathymetry from 10–11 May, the middle of the study period, is used here. At the mouth of the inlet is a shallow semicircular ebb shoal (~800 m radius, 1–2 m deep, red-yellow contours in Figure 1b). Inside the

inlet, there is a 150 m wide, 5 m deep channel (hereinafter referred to as the "channel") on the southwestern edge (blue contours, Figure 1b). In April, this primary channel was dredged across the ebb shoal to a depth of about 2 m below the ambient sand level (yellow contours, Figure 1b). The northeastern side of the inlet mouth is shallow (2 m deep, hereinafter referred to as the "shoals"), with a remnant channel crossing the ebb shoal (yellow-green contours, Figure 1b).

2.2. Instrumentation and Processing

Observations were collected nearly continuously during May 2012. Wave heights and tidal elevations were measured at 2 Hz for 3072 s starting at the top of each hour with stand-alone pressure gages deployed at 12 sites (black symbols, Figure 1b) near and in the inlet mouth. These stand-alone sensors were colocated with either acoustic Doppler velocimeters (ADVs, triangles, Figure 1b) or with acoustic Doppler current profilers (ADCPs, circles, Figure 1b). At all locations with ADVs, the stand-alone pressure gages were buried about 0.10 m below the seafloor to avoid dynamic pressure fluctuations [*Raubenheimer et al*., 2001]. At the channel location, the stand-alone pressure sensor initially (30 April 2012) was mounted on the seafloor and then buried about 0.10 m below the seafloor on 4 May 2012. The resulting shift in mean pressure was accounted for in the processing so that all pressure data are relative to the survey datum. Retaining the 5 days during which the sensor was unburied does not affect the results. Atmospheric pressure was measured at ground level about 5 km inland. Pressure measurements were corrected for atmospheric pressure fluctuations. Water levels were estimated from the near-seafloor pressure measurements assuming hydrostatic pressure and a water density of 1025.6 kg/m^3 (based on salinity of $\sim$36 psu and temperature of $\sim$20°C measured near the inlet mouth in late April 2012). Mean water levels η were estimated by averaging the data from the buried pressure sensors over each 3072 s record. Water depths h were estimated from the mean water levels and the bathymetry. The water-level fluctuations from the near-bottom pressure sensors were corrected to sea-surface elevation fluctuations using linear theory [*Raubenheimer et al*., 1998], and significant wave heights H_{sig} were calculated as four times the standard deviation of the sea-surface elevation fluctuations in the wind-wave frequency (f) band ($0.05 < f < 0.30$ Hz). Accounting for wave-current interactions [*Smith*, 2002] did not significantly affect the wave height or wave forcing estimates.

Flows and wave directions were estimated from measurements with ADVs, which sampled velocity and pressure at 2 Hz for 3072 s starting at the top of every hour, and with ADCPs (see below). The locations of the velocity sample volumes and internal pressure gages for the ADVs were about 0.78 and 0.45 m above the seafloor, respectively. Noisy data from the ADVs (e.g., owing to bio-fouling or bubbles) were removed [*Elgar et al*., 2001, 2005]. The internal pressures from the ADVs are time synced with the velocity, enabling the energy-weighted wave directions in the wind-wave frequency band to be estimated from 3072 s data records [*Kuik et al*., 1988]. Wave directions were rotated to be relative to the along-inlet direction, defined as $-46°$ relative to true north based on a straight line between the offshore and channel sites (Figure 1b). Mean flows were estimated by averaging data over 3072 s records. At the shoals location, the mean flows are representative of the depth-averaged flows [*Wargula et al*., 2013].

Wave directions also were estimated from the upward-looking ADCP at the channel location, which sampled near-surface flows and near-bed pressure at 2 Hz for 1024 s starting at the top of the hour and the half hour. In addition, this instrument measured currents in 0.50 m vertical bins from about 0.70 m above the bed to about 0.50 m below the water surface every minute for 12 min ending on the half hour and hour. Upward-looking ADCPs at other, shallower channel locations measured 1 min mean currents in 0.25 m vertical bins from about 0.45 m above the bed to about 0.25 m below the water surface. Depth-mean and time-mean flows at locations with ADCPs were estimated by averaging over the water depth and over the observations in each hour-long period.

Mean flow measurements from ADVs and ADCPs were rotated into along-inlet and across-inlet directions (positive onshore and to the northeast). Principal flow axes were estimated as [*Emery and Thomson*, 2001]:

$$\theta_p = \frac{1}{2}\tan^{-1}\left[\frac{2\overline{u'_1 u'_2}}{\overline{u'^2_1} - \overline{u'^2_2}}\right] \quad (1)$$

where θ_p is the principal axis angle relative to north, u'_1 and u'_2 are the demeaned east-west and north-south velocity fluctuations, and an overbar indicates time averaging.

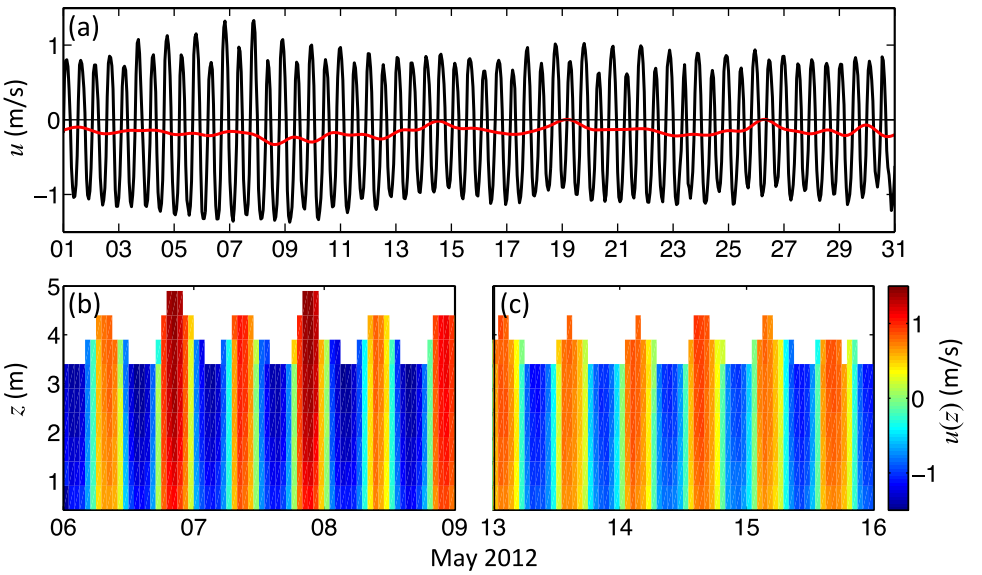

Figure 2. (a) Depth-averaged along-inlet currents, *u* (black curve is unfiltered and red curve is low-pass filtered with the mean retained) and (b and c) unfiltered along-inlet currents, *u*(z) (color contours, scale on the right) at the channel site (black filled circle, Figure 1b) as a function of the distance above the bottom, *z*, versus time during spring (Figure 2b) and neap tides (Figure 2c).

Onsite winds were measured just southwest of the inlet mouth about 4.3 m above mean sea level on a piling located in 2 m water depth (white square, Figure 1b) every 5 min until 21 May. Additional hourly wind measurements were obtained offshore about 3 m above sea level on a buoy in 10 m water depth (NDBC station 41038) 55 km southwest of New River Inlet. The onsite and NDBC wind measurements were correlated ($r^2 \sim 0.7$) with 95% confidence. Measured winds were converted to 10 m winds assuming a logarithmic layer, neutral stability, and a roughness length $z_0 = \alpha u_*^2/g$ [*Charnock*, 1955], where α is a free parameter, u_* is the friction velocity, and g is gravitational acceleration. The results are not sensitive to variations in α over the range $0.008 < \alpha < 0.070$ [*Kraus*, 1972; *Smith*, 1980; *Sempreviva et al*., 1990; *Peña and Gryning*, 2008; *Brown and Wolf*, 2009].

2.3. Observations

Tidal currents in the inlet ranged from −1.5 to 1.5 m/s (Figure 2) and maximum discharge rates at peak ebb and flood were about 700 to 900 m^3/s (not shown). Offshore significant wave heights ranged from 0.5 to 2.5 m (Figure 3a) and centroidal (energy-weighted over the wind wave band ($0.05 < f < 0.30$ Hz)) frequencies ranged from 0.11 to 0.18 Hz (not shown). Offshore centroidal wave directions typically were between 0° and 20° relative to shore normal (defined as −46° relative to true north, see section 2.2). During the nor'easter (15 May, Figure 3) waves approached from about 12° south of shore-normal and during the tropical storm on 26 May (Figure 3) waves approached from about 0°. Refraction resulted in approximately 10° changes in wave directions around the semicircular ebb shoal. Wind speeds ranged from 0 to 16 m/s (Figure 3b) and wind directions were most frequently from the south or southwest (not shown).

The along-inlet flows were nearly depth-uniform above the bottom boundary layer (Figures 2b and 2c). The dominant tidal constituent was the M_2 (semidiurnal lunar) tide. Although New River Inlet is a short channel relative to the tidal wavelength (the ratio of channel length to a quarter of a tidal wavelength is about 0.3) [*Li and O'Donnell*, 2005], the tides are progressive with peak ebbs (floods) occurring within about 30 min of low (high) water levels (Figures 2b and 2c) [*MacMahan et al*., 2014]. Similar to prior observations in curved channels [*Waterhouse and Valle-Levinson*, 2010], during flood the maximum flows were approximately centered in the primary channel, whereas during ebb the strongest flows were adjacent to the southwestern shore (Figure 4). During the flood, water funneled into the mouth with weak, fairly uniform magnitude across the inlet width, converging as the inlet width narrowed, consistent with theory [*Stommel and Farmer*, 1952]. The converging flows led to rapid flood flow accelerations near the mouth of the inlet. During the ebb, water exited the inlet mouth in two distinct jets, one in the deep channel and the other in the

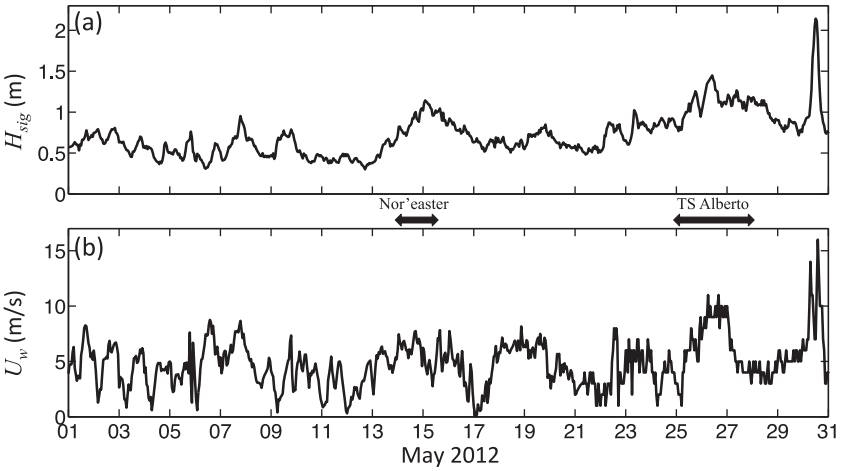

Figure 3. (a) Significant wave heights, H_{sig}, at the offshore site (black filled triangle just offshore of the ebb shoal in 5 m depth, Figure 1b) and (b) local wind speed, U_w, (measured at the white square, Figure 1b) versus time. Times of a nor'easter and tropical storm Alberto are indicated with black arrows. Centroidal wave periods ranged from 5 to 9 s.

shallower remnant channel, with nearly constant flow magnitudes across the ebb shoal. The principal axes (equation (1)) of flood and ebb differ by about 10° to 20° [*Wargula et al.*, 2013] (Figure 4).

Principal flow axes (equation (1)) vary along the inlet (cross shore), as well as across the inlet width (Figure 4). Near the inlet mouth, the major axis flow direction varies from about −30° to −60°, depending on tidal stage and location. The results are not sensitive to changes in the definition of the along-inlet direction for $-60° < \theta < -15°$ [*Wargula et al.*, 2013].

3. Theory: Momentum Balance

The effects of wave forcing on along-inlet flows at New River Inlet were examined by analyzing the dominant terms in the depth-integrated momentum balance [*Lentz et al.*, 1999; *Cáceres et al.*, 2003; *Hench and Luettich*, 2003]

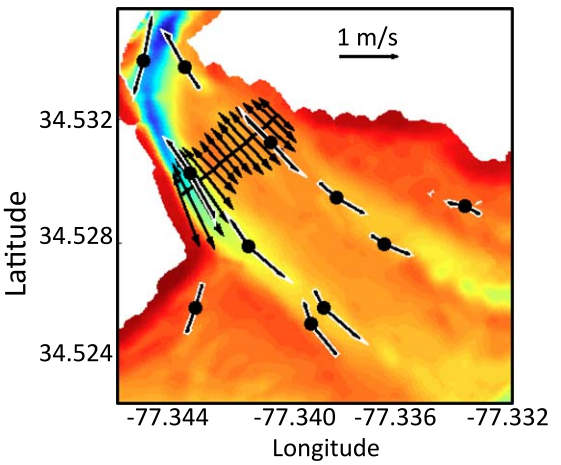

Figure 4. Plan view of New River Inlet. Colors are water depth contours (see Figure 1b for color scale) and arrows are principal axes for flood and ebb flows. The length of each arrow is the average flood or ebb magnitude over the study period (a 1 m/s scale arrow is shown near the top center). Black arrows highlighted in white are calculated from in situ sensors located at the corresponding black circle. Black arrows without white highlighting are calculated from boat-mounted current profiles (see Appendices A and B) that were depth and horizontally averaged over 30 m cross-inlet sections along the black line across the inlet.

$$\frac{\partial(hu)}{\partial t}+\frac{\partial(hu^2)}{\partial x}+\frac{\partial(huv)}{\partial y}-Fhv=-\frac{h}{\rho_0}\frac{\partial P_b}{\partial x}+\frac{\tau^{sx}}{\rho_0}-\frac{\tau^{bx}}{\rho_0}-\frac{1}{\rho_0}\frac{\partial S_{xx}}{\partial x}-\frac{1}{\rho_0}\frac{\partial S_{xy}}{\partial y} \quad (2)$$

where t is time, x and y are the along-inlet and across-inlet coordinates, h is water depth, u and v are the along-inlet and across-inlet components of the depth-averaged velocity, F is the Coriolis parameter, ρ_0 is water density, P_b is the bottom pressure (which is simplified by the constant-density hydrostatic equation $P_b = \rho_0 g\eta$, where η is the mean water level), τ^{sx} is wind stress (approximated by $\rho_a C_w u_w |U_w|$, where C_w is the wind drag coefficient [*Large and Pond*, 1981], u_w is the along-inlet wind speed and $|U_w|$ is the total wind speed at 10 m above the water surface, and ρ_a is the air density), and τ^{bx} is bottom stress (approximated by $\rho_0 C_D u|U|$, where C_D is the bottom drag

coefficient calculated from the data (see section 4 and Figure 7) and $|U|$ is the total velocity magnitude $\sqrt{u^2+v^2}$)). The results are not sensitive to the small (less than 5%) changes in water depth h owing to the (neglected) erosion and accretion at the sensor locations. The cross-shore and diagonal wave radiation stresses S_{xx} and S_{xy} are approximated as [*Longuet-Higgins and Stewart*, 1964; *Raubenheimer et al*., 2001; *Apotsos et al*., 2008]

$$S_{xx}=E_w\left[(\cos^2\theta_b+1)\frac{c_g}{c}-\frac{1}{2}\right] \tag{3}$$

$$S_{xy}=E_w\cos\theta_b\sin\theta_b\frac{c_g}{c} \tag{4}$$

where θ_b is the centroidal wave direction, c_g and c are the group velocity and phase speed (estimated from the centroidal frequency and the water depth), and E_w is the wave energy, calculated as:

$$E_w=\frac{1}{16}\rho_0 g H_{sig}^2 \tag{5}$$

The results are not sensitive to the small differences (roughly 10–15% overestimation during large wave events) between radiation stresses estimated using the bulk formulas above and radiation stresses estimated using a frequency-dependent directional moment technique [*Herbers and Guza*, 1990; *Elgar et al*., 1994; *Raubenheimer et al*., 2001; *Feddersen*, 2004].

To focus on how wave forcing (rather than tidal processes) affects the flows, all momentum balance terms were demeaned (see section 5) and low-pass filtered (e.g., red curve in Figure 2a) using a discrete Fourier transform filter (cutoff period of 30 h) with three transition band samples [*Rabiner and Gold*, 1975, Table X]. The results are not sensitive to cutoff periods ranging from about 26 to 40 h. Owing to ringing artifacts (Gibbs phenomenon) associated with filtering, roughly 24 h of data were removed from the beginning and end of the time series. The conclusion that waves affect the flows in the inlet is not sensitive to the removal of these data. The subtidal pressure and flow measurements include astronomically forced fortnightly tidal fluctuations and fluctuations at subtidal frequencies driven by nonlinear interactions between higher frequency tidal processes [*Fortunato et al*, 1999; *MacMahan et al*., 2014]. Storm-driven fluctuations at tidal frequencies, which can result from short period changes in the forcing or from nonlinear interactions between the forcing processes (e.g., waves and winds) and the tidal flows [*Brown et al*., 2012] are neglected. Thus, the effects of storm processes may be underestimated.

Coriolis acceleration is neglected because the Rossby number is large at the inlet. Subtidal temporal changes in flux and alongshore gradients of wave radiation stress (the first and last terms in equation (2), $O(10^{-5})$ m^2/s^2, Figure 5) were significantly smaller than the other terms and also are neglected. Remote and local winds may cause subtidal motions at inlets [*Wong and Moses-Hall*, 1998; *Wong and Valle-Levinson*, 2002]. The effects of large-scale wind forcing, which likely is important to the flows in the inlet [*Geyer*, 1997; *Brown et al*., 2013; *Li*, 2013], are included in the forcing. At New River Inlet, local wind stress is weakly correlated with the measured pressure gradients, which include setup and surge owing to local and remote winds. However, observation-based estimates suggest that local wind stresses ($O(10^{-5})$ m^2/s^2, pink curve, Figure 5) over the km-wide ebb shoal are uncorrelated with the bottom stress, and, consistent with prior surfzone studies [*Lentz et al*., 1999] are an order of magnitude smaller than the wave forcing term ($O(10^{-4})$ m^2/s^2, blue curve, Figure 5). Sensitivity tests indicate that local radiation-stress gradients are much larger than local wind stresses for a range of sea-surface roughnesses ($0.008<\alpha<0.070$) [*Brown and Wolf*, 2009] and wind drag coefficients ($0.0010<C_w<0.0025$). Previous models have shown that inlet dynamics differ between the channel and shoals [*Cáceres et al*., 2003; *Buijsman and Ridderinkhof*, 2007; *Waterhouse and Valle-Levinson*, 2010; *Olabarrieta et al*., 2011], and thus the channel and shoal momentum balances are examined separately.

Accelerations of the inlet flows between the offshore and inlet sites (Figure 4) could affect the subtidal momentum balance via the advective acceleration terms [*Hench et al*., 2002; *Cáceres et al*., 2003; *Hench and Luettich*, 2003; *Li and O'Donnell*, 2005; *Winant*, 2008; *Waterhouse and Valle-Levinson*, 2010; *Tutak and Sheng*, 2011]. However, consistent with prior modeling studies in well-mixed, shallow, tidal estuaries, rough estimates suggest the two horizontal advection terms in the channel partially cancel (see Appendix A), and

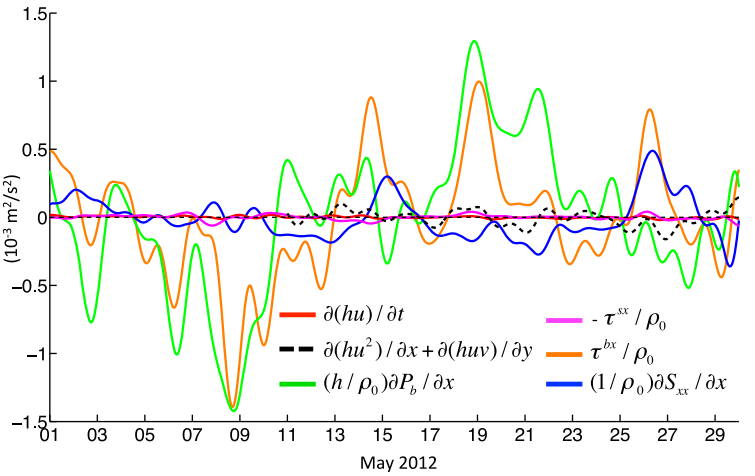

Figure 5. Subtidal, demeaned channel momentum balance terms (equation (1)): temporal change in flux (red curve), advective acceleration (black dashed curve, Figure 6), pressure gradient (green curve), local wind stress (pink curve), bottom stress (orange curve), and wave radiation stress gradient (blue curve) versus time.

their sum (black dashed curve, Figures 5 and 6) appears to be small ($O(10^{-5}$ to $10^{-4})$ m^2/s^2) compared with the dominant ($O(10^{-3})$ m^2/s^2) momentum balance terms [*Jay*, 1991; *Olabarrieta et al*., 2011]. Furthermore, addition of these terms to the subtidal momentum balance does not change the overall correlations between the momentum balance terms (r^2 changes less than 2%, see section 4) or the best fit value of the drag coefficient (C_D changes are order 2%, see Figure 7 and section 5.3). Also consistent with prior studies [*Li and O'Donnell*, 2005; *Winant*, 2008; *Waterhouse and Valle-Levinson*, 2010; *Olabarrieta et al*., 2011], depth-averaged lateral advection was smaller on the shoals than in the channel (Appendix A and Figure A2). Estimates of the advective terms are less accurate at the shoals location, owing to their relatively smaller magnitudes and to curvature of the remnant channel. When crude calculations of the advective terms on the shoals are added to the momentum balance, the overall correlation and drag coefficient are reduced by about 10% and 20–25%, respectively. However, these reductions do not change the conclusions, and thus, these terms are neglected here.

The simplified, subtidal, along-inlet, depth-integrated momentum balance becomes:

$$C_D u|U| \approx \frac{\tau_{bx}}{\rho_0} = -gh\frac{\partial \eta}{\partial x} - \frac{1}{\rho_0}\frac{\partial S_{xx}}{\partial x} \tag{6}$$

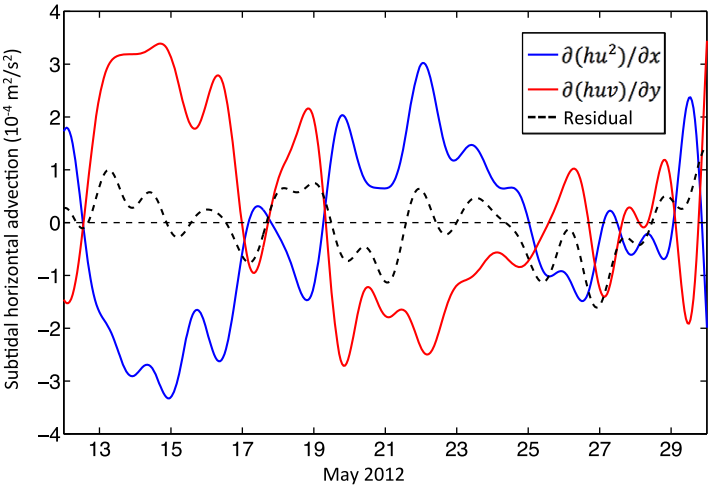

Figure 6. Subtidal horizontal advection terms (second (blue curve) and third (red curve) terms in equation (2)) and the sum of the two terms (dashed black curve) in the channel versus time. See Appendix A for methods.

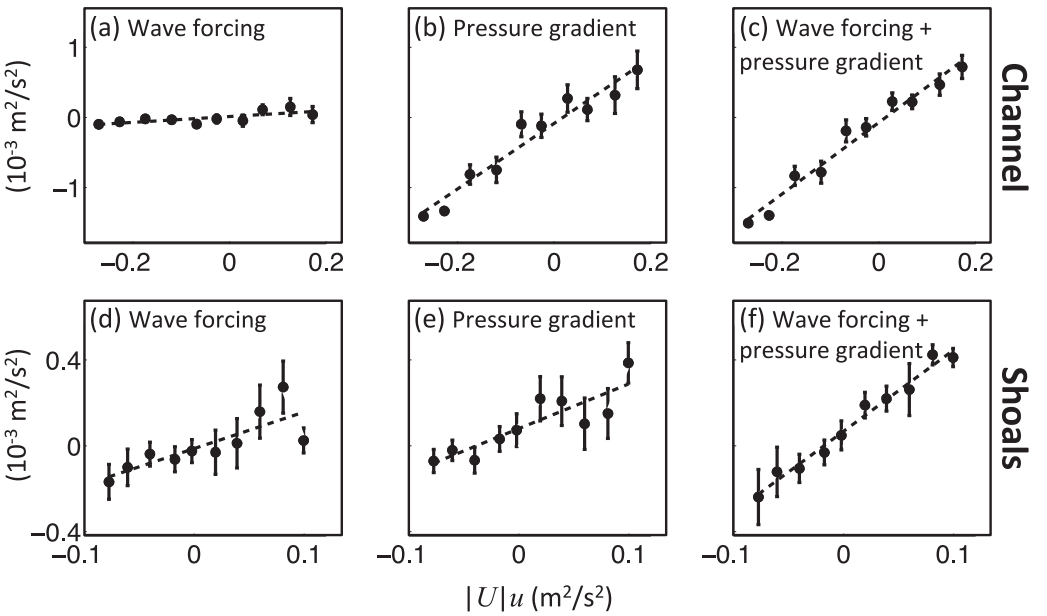

Figure 7. Binned means (circles) and standard deviations (vertical bars) of along-inlet (a and d) wave radiation-stress gradients, (b and e) pressure gradients, and (c and f) sum of along-inlet wave radiation-stress and pressure gradients versus inlet flow ($|U|u$) in the (a–c) channel and on the (d–f) shoals. The dashed lines are least squares linear fits to the binned values. Drag coefficients C_D calculated from the linear fits are 0.005 in the channel (Figure 7c) and 0.004 on the shoals (Figure 7f). Note the vertical ranges are larger for the channel (Figures 7a–7c) than for the shoals (Figures 7d–7f).

The water depth h was approximated as 5 m at the channel and 2 m on the shoals. The root-mean-squared subtidal changes in mean water level $\partial\eta$ between the offshore site and the channel and the shoals were 0.02 m and 0.01 m, respectively. Root-mean-squared subtidal flows were 0.17 m/s in the channel (red curve, Figure 2a) and 0.10 m/s on the shoals. Spatial gradients were calculated using a forward derivative with ∂x the measured distance between the offshore location and the channel or shoals site (approximately 1000 m, Figure 1b). The difference between the distance from the shoals to 5 m depth in the along-inlet direction and the distance from the shoals to the offshore sensor is about 30 m (less than 3%) and does not affect the results. Computing the gradients in the momentum balance using a forward difference assumes that the terms vary linearly between the two sensors. The simple balance (equation (6)) is similar for centered differences using observations collected farther upstream (not shown), supporting this assumption.

The sensor array used here can resolve large-scale (O(few-hundred m)) forcing and circulation patterns, but not small-scale ($O(<100$ m)) features that may be caused by unresolved bathymetric variations, or by small-spatial and short-temporal fluctuations in the radiation stresses. For example, visual observations during the field study, and preliminary results from remote sensing [*Jessup et al.*, 2012] and drifting instruments [*Zippel and Thomson*, 2012] suggest that wave dissipation was spatially variable. Although these small-scale fluctuations may contribute to scatter in the simple momentum balance used here, their inclusion would not change the conclusion that wave forcing contributes significantly to the observed flows.

4. Results

Between the offshore and the deep channel locations (Figure 1b), subtidal bottom stress is primarily balanced by subtidal pressure gradients ($r^2 = 0.96 \pm 0.02$, Figure 7b), similar to the tidal balance expected in the straits of long, narrow inlets [*Hench et al.*, 2002]. The pressure gradient fluctuations (green curve, Figures 8a and 9a) may result from fortnightly oscillations, remote- or large-scale-wind forcing, and other subtidal motions in the ocean that propagate into the inlet and the ICW and from subtidal motions that are generated in the inlet via nonlinear interactions between tidal constituents [*Chant*, 2001; *MacMahan et al.*, 2014].

In the main channel, wave forcing is an order of magnitude smaller than the pressure gradient (Figures 7a, 7b, and 8a) and does not improve the overall balance significantly when summed with the pressure

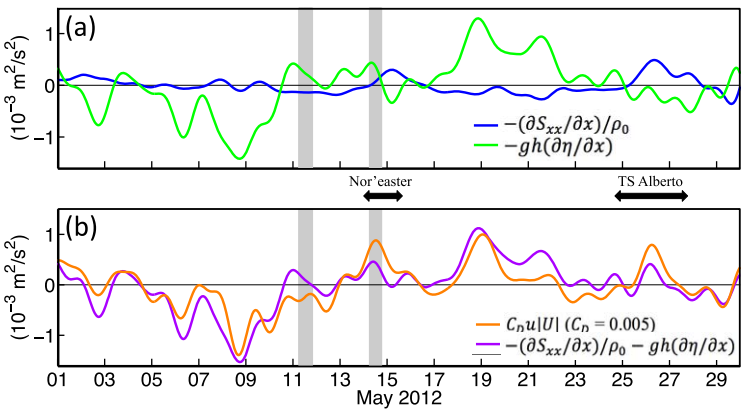

Figure 8. Subtidal, demeaned channel (a) wave forcing $-(\partial S_{xx}/\partial x)/\rho_0$ (blue curve) and pressure gradient $-gh(\partial\eta/\partial x)$ (green curve) and (b) bottom stress (orange curve, $C_D = 0.005$, from Figure 7c) and wave radiation-stress plus pressure gradients $-(\partial S_{xx}/\partial x)/\rho_0 - gh(\partial\eta/\partial x)$ (purple curve) versus time. The two curves in Figure 8b are correlated ($r^2 \sim 0.68$) at 95% confidence levels. Gray vertical stripes are times of cross-inlet transects (white line, Figure 1b) with the boat-mounted current profiler (see Appendices A and B). Times of a nor'easter and tropical storm Alberto are indicated with black arrows.

gradient (compare $r^2 = 0.98 \pm 0.01$, Figure 7c, with $r^2 = 0.96 \pm 0.02$, Figure 7b), although the standard deviations in each bin are reduced. However, even though wave forcing usually was relatively small, during big wave events the radiation-stress gradient term became larger than the pressure gradient (see black arrows indicating nor'easter and tropical storm Alberto, Figure 8a), and was needed to balance the bottom stress (Figure 8b).

Between the offshore and shallow shoals sites (Figure 1b), wave radiation-stress and pressure gradients have similar magnitudes (Figures 7d, 7e, and 9a) and each are correlated with bottom stress ($r^2 = 0.65 \pm 0.13$, Figure 7d, and $r^2 = 0.75 \pm 0.10$, Figure 7e). Including both terms improves the correlation between forcing and bottom stress significantly ($r^2 = 0.98 \pm 0.01$, Figure 7f).

Discrepancies between the estimated bottom stress and the sum of the forcing terms (Figures 8b and 9b) could be owing to neglected processes (e.g., wind stress and nonlinear advection), three-dimensional effects (e.g., eddies), estimation techniques (e.g., forward differences and filter errors), and measurement errors.

During storms (black arrows at 15 May and 25–27 May in Figures 8b and 9b), the wave forcing term enhances the flood flows into the inlet (bottom stress is positive) against an adverse (negative) pressure gradient.

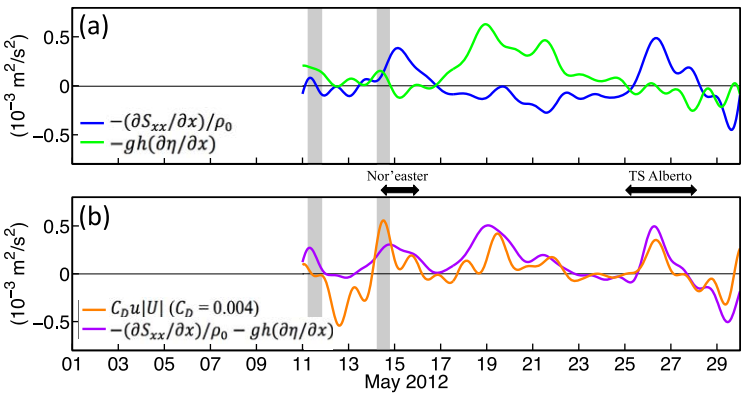

Figure 9. Subtidal, demeaned shoals (a) wave forcing $-(\partial S_{xx}/\partial x)/\rho_0$ (blue curve) and pressure gradient $-gh(\partial\eta/\partial x)$ (green curve) and (b) bottom stress (orange curve, $C_D = 0.004$, from Figure 7f) and wave radiation-stress plus pressure gradients $-(\partial S_{xx}/\partial x)/\rho_0 - gh(\partial\eta/\partial x)$ (purple curve) versus time. The two curves in Figure 9b are correlated ($r^2 \sim 0.45$) at 95% confidence levels. Gray vertical stripes are times of cross-inlet transects (white line, Figure 1b) with the boat-mounted current profiler (see Appendices A and B). Times of a nor'easter and tropical storm Alberto are indicated with black arrows.

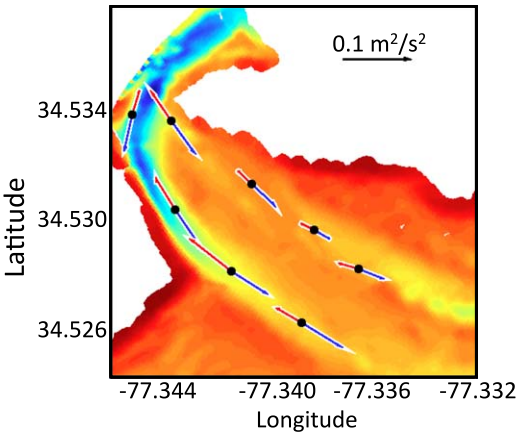

Figure 10. Plan view of New River Inlet. Colors are water depth contours (see Figure 1b for color scale) and arrows are directions and magnitudes of demeaned subtidal $u|U|$ at in situ sensors, averaged over times with significant wave heights less than (blue arrows) and greater than (red arrows) 1 m. A 0.1 m^2/s^2 scale arrow is shown near the top right.

Local flows ($u|U|$) at in situ sensors upstream and downstream of the locations used in the momentum balance calculations also showed enhanced flood flows during times with bigger waves (Figure 10). Additionally, the tidally averaged discharge (not shown) measured by a boat-mounted current profiler across the inlet width (white line, Figure 1b) is consistent with the result that wave forcing enhances flood flows (see Appendix B).

5. Discussion

5.1. Wave-Enhanced Fluxes in the Inlet

These observation-based estimates of wave-enhanced onshore (flood) flows are consistent with prior model simulations of Óbidos Inlet and Lagoon, Portugal [*Bertin et al*., 2009; *Malhadas et al*., 2009] and of the shoals and shallow channels at Ría de Ribadeo, Spain [*Piedracoba et al*., 2005] and Willapa Bay Inlet, WA [*Olabarrieta et al*., 2011]. However, at Ría de Ribadeo the ebb flows were enhanced on the western side of the channel during large waves, and at Willapa Bay the ebb jet in the main channel was narrowed and intensified by the action of the waves. The enhancement of the flood flows seen in the main channel at New River Inlet could be owing to differences in the inlet geometry (e.g., asymmetric wave breaking patterns at Ría de Ribadeo and Willapa Inlet), or to the time needed to reach a steady state.

The Ría de Ribadeo is a closed system with a relatively large inlet (width $\sim$ 1 km and depth $\sim$ 17 m) connected to a small embayment (area $\sim$ 8.5 km^2). During storms, wave breaking over the shoals on the eastern side forces flows into the inlet. The small embayment quickly reaches a steady state, and a circulation pattern is initiated with the onshore fluxes balanced by enhanced ebb flows on the western side of the inlet [*Piedracoba et al*., 2005]. Willapa Bay (area $\sim$ 260 km^2) also is a closed system that has a large inlet (width about 10 km) with a deep ($\sim$ 24 m) main channel on the northern side and shoals interrupted by several shallow channels on the southern side. Wave breaking over the extensive shoals is predicted to drive flows into the inlet, causing an 11.8% increase in bay volume [*Olabarrieta et al*., 2011]. As a steady state is approached (with wave forcing balanced at least partly by the setup in the bay), the enhanced flows into the inlet over the shoals [e.g., *Olabarrieta et al*., 2011, red and yellow areas in Figure 14) may be balanced by reduced flood and enhanced ebb flows in the main channel [e.g., *Olabarrieta et al*., 2011, blue areas in Figure 14]. Similar to Ría de Ribadeo, the asymmetry of the wave forcing over the spatially nonuniform Willapa Bay shoal-channel system, in combination with local conservation of mass across the inlet, may contribute to the spatial variability of the flows. Although Óbidos lagoon (area $\sim$ 7 km^2) also is a closed system, the inlet is narrow ($\sim$ 25 m) and shallow ($\sim$ 1 m) [*Malhadas et al*., 2009], possibly restricting the wave-driven flux of water into the lagoon and increasing the time during which there is a net mass flux into the bay, allowing inflow across the entire width of the inlet. New River Inlet is an open system, connected to other inlets via the ICW (Figure 1a), and with relatively symmetric wave forcing around the semicircular ebb shoal (Figure 1b). The additional inlets along the ICW allow for water mass exchange and leakage. Thus, roughly uniform wave forcing during storms may enhance net flood flows throughout the inlet without local conservation of mass or asymmetric intensification of flows.

5.2. Tidally Averaged Flows

Here "residual" flows are estimated crudely by averaging over all full tidal cycles in the time series. The results are not significantly different (less than 0.01 m/s change) from those obtained by subtracting the astronomically forced tidal motions estimated with a harmonic analysis from the full time series and averaging over the experiment period. These longer period, tidally averaged motions underlying the subtidal fluctuations analyzed above may be owing to nonlinear interactions between tidal motions, to inlet processes with periods greater than a few days [*Brown et al*., 2012], or to exchanges with other inlets connected via the ICW.

At New River Inlet, tidally averaged (over 18 to 30 days) flows are ebb-dominant ($O(-0.1$ m/s)) at both the channel and shoal locations within the inlet mouth (Figure 4). However, farther upstream, near the first 90° bend, and where the width of the inlet narrows (Figure 1b), the tidally averaged flows on the shoals become flood dominant [*Lippmann et al*., 2013] (compare length of flooding and ebbing arrows in Figure 4 at the most upstream location on the shoals).

The tidally averaged flows are not included in the momentum balance analysis above (sections 3 and 4). Combining the tidally averaged and subtidal flows shows that, during storms, wave forcing retarded or reversed the offshore-directed "nontidal" flows at all locations. In the main channel, flows were reversed to onshore-directed near the 90° bend, retarded to nearly zero inside the inlet mouth (filled black circle, Figure 1b), and retarded to a smaller, though still offshore-directed, magnitude in locations offshore of the mouth and across the ebb shoal. A similar along-inlet gradient in flow response during large wave events was observed on the shoals. However, the location of flow retardation to near zero was farther offshore than that in the main channel (between the filled triangle inside the inlet and the open triangle just offshore, Figure 1b). The onshore (or less offshore) directed "nontidal" flow at all locations in the channel and on the shoals during storm events supports the result that waves enhanced flows into the inlet.

5.3. Estimated Drag Coefficients

The 95% confidence limits on C_D estimated using a least squares fit are small (< 0.0001). However, shortening or lengthening the section of data used in the analysis and changing the bin sizes (Figure 7) can change the estimate of C_D by as much as $\pm$ 0.002, possibly owing to errors and neglected processes associated with the filtering technique [*Brown et al*., 2012] or to temporal variations in the bottom stress or other processes. For example, previous studies have suggested that waves may increase or decrease the apparent bed roughness, depending on the wave and current directions, water depth, and the wave amplitude [*Grant and Madsen*, 1979; *Olabarrieta et al*., 2010]. At inlets with significant wave forcing, storm-related variations in wave conditions and tidal-modulation of currents, wave heights, and wave breaking may lead to a temporally varying bottom stress [*Kang and Di Iorio*, 2006]. Drag coefficient values fitted separately to ebb and flood conditions suggest that the bottom drag is smaller during floods and larger during ebbs. Using these different ebb and flood C_D values slightly improves the correlations between the bottom stress and forcing on the shoals. Temporal variations in these bulk estimates of C_D based on the simplified momentum balance also could be owing to changes in flow patterns and migrating bed forms, or to neglected processes such as time-varying wave breaking induced turbulence [*Feddersen et al*., 2004], lateral mixing and eddies [*Geyer et al*., 2000], and unresolved advection [*Brown and Trask*, 1980; *Geyer et al*., 2000].

Despite these limitations in the estimates and the uncertainties in the value of the drag coefficients, the C_D on the shoals is lower than the C_D in the channel irrespective of the length of time series used, the combination or separation of ebb and flood, or the fitting to binned or unbinned momentum terms. Gravel and bed forms larger in the channel than on the sandy shoals (P. Traykovski, personal communication, 2012) may contribute to the higher C_D in the channel. The different C_D estimation techniques do not change the qualitative results that wave forcing enhances flood flows in the inlet.

6. Conclusions

Observations of tides, waves, and currents in both a 5 m deep main channel and a shallower, 2 m deep remnant channel on the neighboring shoals at New River Inlet, NC indicate that wave forcing is a significant contribution to the subtidal along-channel momentum balance. Within the main inlet channel, the primary force balance is between the pressure gradient and bottom stress, with wave radiation stresses significant only during storms. On the shallower shoals, wave radiation-stress and pressure gradient forcing contribute equally to the balance with bottom stress. Wave forcing tends to enhance the flood flows at the inlet, both in the channel and on the shoals.

Appendix A: Advection Terms

The magnitudes of the two subtidal advection terms (second and third terms in equation (2)) are estimated crudely using the in situ data (Figure 6). The along-inlet gradient $\partial(hu^2)/\partial x$ (blue curve, Figure 6) is estimated by a forward difference between hu^2 at the offshore and the channel or shoals sites (black filled circle and triangles, Figure 1b) divided by the distance between the sites. The cross-inlet gradient $\partial(huv)/\partial y$

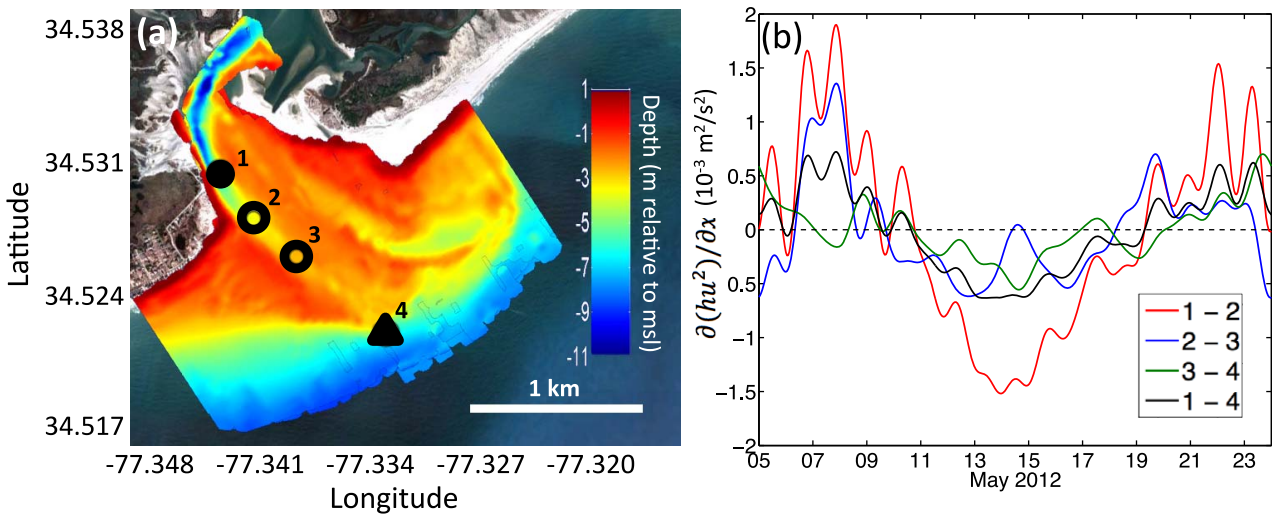

Figure A1. (a) Locations of instruments (latitude and longitude indicated on axes) used to form sensor pairs to estimate (b) the subtidal along-inlet gradient of along-inlet advection $\partial(hu^2)/\partial x$ (second term in equation (2)) as a function of time. Filled circle and triangle are "channel" and "offshore" sites. Pair 1–4 (black curve in Figure A1b) was used in the final advection calculation (blue curve, Figure 6).

in the channel (red curve, Figure 6) is estimated by a forward difference between *huv* at the channel and shoals sites divided by the distance between them. The two terms are correlated ($r^2 = 0.91$) with 95% confidence, but are out of phase, and thus roughly balance each other. In particular, the sum of the two advection terms is smaller than the dominant forcing terms (compare black dashed curve with the orange, green, and blue curves, Figure 5).

The accuracy of the advection estimates, which are based on spatially sparse measurements, is evaluated using additional in situ measurements spanning the ebb shoal, and using high-spatial resolution boat-mounted current profiler-transect measurements (white line, Figure 1b). Estimates of the subtidal along-inlet gradient $\partial(hu^2)/\partial x$ in the channel between different instrument pairs along the inlet (1–2, 2–3, 3–4, Figure A1a) shows that the magnitude of the advective term increased onshore. All estimates showed a similar structure in time (Figure A1b), suggesting that the estimates are plausible. Although using the channel (sensor 1, Figure A1a) and offshore (sensor 4, Figure A1a) locations may result in underestimation of the advective term by about a factor of 3 (compare 1–4 with 1–2, Figure A1b), these sensors were used in the analysis to be consistent with estimates of the other momentum terms.

Boat-mounted profiler transects suggest that the underestimation of the along-inlet term $\partial(hu^2)/\partial x$ may be balanced by similar underestimation of the cross-inlet term $\partial(huv)/\partial y$. Current profile transects (white line, Figure 1b) were conducted hourly for 14 h on 11 and 14 May to sample the change in flows over a complete tidal cycle. The downward-facing transducer was positioned 0.20 m below the water surface and sampled at 1 Hz with vertical bins from 0.02 to 0.50 m and blanking distances of 0.20 to 0.50 m, depending on the water depth (measured by a separate vertical acoustic beam) and velocity conditions. Boat velocity and position were measured by GPS with real-time kinematic corrections. The current profile transects were depth-averaged and horizontally averaged over 20 m (Figure A2) or 30 m (Figure 4) cross-inlet sections. The cross-inlet advection term estimated from these high-spatial resolution transects is maximum in the channel and small over the shoals (Figure A2), consistent with prior studies [*Li and O'Donnell*, 2005; *Winant*, 2008; *Waterhouse and Valle-Levinson*, 2010; *Olabarrieta et al.*, 2011]. In particular, in the channel (cross-inlet distance −20 to 100 m, Figure A2) the advection term is large ($O(10^{-4}$ to 10^{-3} m^2/s^2)) and negative for both ebbing and flooding flows. On the shoals, the cross-inlet term fluctuates between positive and negative, but always is small. The signs and relative magnitudes of the crude estimates from the in situ sensors are consistent with the transect-based estimates. However, the in situ-based estimates (Figure 6) are more than a factor of 4 smaller than the local estimates from the transect data owing primarily to the poor spatial resolution of the in situ measurements, which average the terms between the instrument locations (between the symbols in Figure A2).

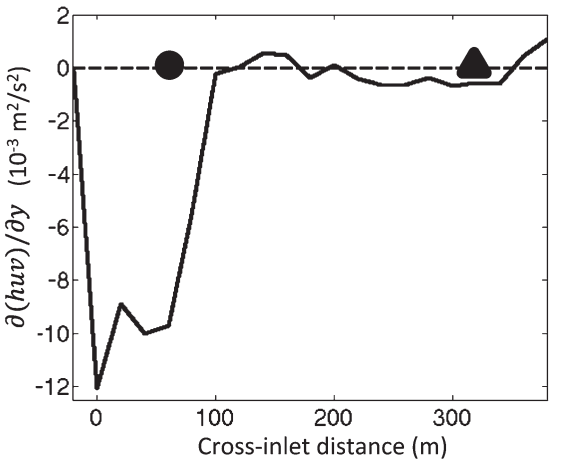

Figure A2. The tidally averaged cross-inlet gradient of along-inlet advection $\partial(huv)/\partial y$ (third term in equation (2)) calculated from 20 m horizontally binned flows and water depths measured by the boat-mounted current profiler across the inlet width (white line, Figure 1b) versus cross-inlet distance. The origin (0 m) of the cross-inlet distance was set at the deepest point in the channel. The black circle and triangle on the dashed line at advection = 0 are the locations of the channel and shoals in situ sensors (Figure 1b).

Appendix B: Tidally Averaged Discharge

Discharge was calculated by spatially integrating the boat-mounted current profile transects (see Appendix A) over the inlet cross-section (white line, Figure 1b). To calculate the tidally averaged discharge during specific periods, the hourly discharge data were interpolated using a spline fit and integrated in time.

The tidally averaged discharge measured on 11 and 14 May by the boat-mounted current profiler across the inlet width is consistent with the result that wave forcing enhances flood flows (see section 4). On 11 May, during calm conditions (H_{sig} = 0.5 m and light northerly winds $\sim$ 4 m/s (Figure 3) from $\sim$ 0°), the averaged discharge was out of the inlet (ebbing). However, on 14 May, during an approaching storm (H_{sig} = 1.0 m and moderate southerly winds $\sim$ 6 m/s (Figure 3) from $\sim$ 170°), the averaged discharge was into the inlet (flooding). In addition to wave forcing, the southerly winds may have contributed to the residual flooding discharge. Note that the subtidal pressure gradient was similar on both days (green curves in Figures 8a and 9a).

Acknowledgments

We thank the PVLAB field crew for their hard work, persistence, good humor, and efforts in less-than-pleasant conditions to collect this data set, Jesse McNinch and the staff of the US Army Corps of Engineers Field Research Facility for providing bathymetry and assisting with instrument deployment, Jim Thomson for the onsite wind data, and the Coastal Ocean Research and Monitoring Program (Station 41038) for offshore wind data. We had many useful discussions with Jamie MacMahan, Tom Hsu, Julie Chen, Rocky Geyer, and Peter Traykovski about subtidal pressure fluctuations, bottoms stresses, and bed forms at New River Inlet. Maitane Olabarrieta and the anonymous reviewer are thanked for numerous helpful suggestions that improved the manuscript. The data used in this publication are available by contacting Britt Raubenheimer (britt@whoi.edu) or Steve Elgar (elgar@whoi.edu). Funding was provided by the Office of Naval Research, the Office of the Assistant Secretary of Defense for Research and Engineering, and a National Defense Science and Engineering Graduate Fellowship.

References

Apotsos, A., B. Raubenheimer, S. Elgar, R. T. Guza, and J. A. Smith (2007), Effects of wave rollers and bottom stress on wave setup, *J. Geophys. Res.*, *112*, C02003, doi:10.1029/2006JC003549.

Apotsos, A., B. Raubenheimer, S. Elgar, and R. T. Guza (2008), Wave-driven setup and alongshore flows observed onshore of a submarine canyon, *J Geophys. Res.*, *113*, C07025, doi:10.1029/2007JC004514.

Aubrey, D. G., T. R. McSherry, and P. P. Eliet (1993), Effects of multiple inlet morphology on tidal exchange: Waquoit Bay, Massachusetts, *Coastal Estuarine Stud.*, *44*, 213–235.

Bertin, X., A. B. Fortunato, and A. Oliveira (2009), A modeling-based analysis of processes driving wave-dominated inlets, *Cont. Shelf Res.*, *29*, 819–834, doi:10.1016/j.csr.2008.12.019.

Blanton, J. O., G. Lin, and S. A. Elston (2002), Tidal current asymmetry in shallow estuaries and tidal creeks, *Cont. Shelf Res.*, *22*, 1731–1743, doi:10.1016/S0278-4343(02)00035-3.

Boon, J. D., and R. J. Byrne (1981), On basin hypsometry and the morphodynamic response of coastal inlet systems, *Mar. Geol.*, *40*, 27–48, doi:10.1016/0025-3227(81)90041-4.

Brown, J. M., and J. Wolf (2009), Coupled wave and surge modelling for the eastern Irish Sea and implications for model wind-stress, *Cont. Shelf Res.*, *29*(10), 1329–1342, doi:10.1016/j.csr.2009.03.004.

Brown, J. M., R. Bolaños, M. J. Howarth, and A. J. Souza (2012), Extracting sea level residual in tidally dominated estuarine environments, *Ocean Dyn.*, *62*, 969–982, doi:10.1007/s10236-012-0543-7.

Brown, J. M., R. Bolaños, and J. Wolf (2013), The depth-varying response of coastal circulation and water levels to 2D radiation stress when applied in a coupled wave-tide-surge modelling system during an extreme storm, *Coastal Eng.*, *82*, 102–113, doi:10.1016/j.coastaleng.2013.08.009.

Brown, W. S., and R. P. Trask (1980), A study of tidal energy dissipation and bottom stress in an estuary, *J. Phys. Oceanogr.*, *10*, 1742–1754, doi:10.1175/1520-0485(1980)010<1742:ASOTED>2.0.CO;2.

Buijsman, M. C., and H. Ridderinkhof (2007), Long-term ferry-ADCP observations of tidal currents in the Marsdiep inlet, *J. Sea Res.*, *57*, 237–256, doi:10.1016/j.seares.2006.11.004.

Cáceres, M., A. Valle-Levinson, and L. Atkinson (2003), Observations of cross-channel structure of flow in an energetic tidal channel, *J. Geophys. Res.*, *108*, 3114, doi:10.1029/2001JC000968.

Chant, R. J. (2001), Tidal and subtidal motion in a shallow bar-built multiple inlet/bay system, *J. Coastal Res.*, SI(32), 102–114.

Charnock, H. (1955), Wind stress on a water surface, *Q. J. R. Meteorol. Soc.*, *81*, 639–640, doi:10.1002/qj.49708135027.

Dodet, G., X. Bertin, N. Bruneau, A. B. Fortunato, A. Nahon, and A. Roland (2013), Wave-current interactions in a wave-dominated tidal inlet, *J. Geophys. Res.*, *118*, 1587–1605, doi:10.1002/jgrc.20146.

Elgar, S., T. H. C. Herbers, and R. T. Guza (1994), Reflection of ocean surface gravity waves from a natural beach, *J. Phys. Oceanogr.*, *24*, 1503–1511, doi:10.1175/1520-0485(1994)024<1503:ROOSGW>2.0.CO;2.

Elgar, S., B. Raubenheimer, and R. T. Guza (2001), Current meter performance in the surf zone, *J. Atmos. Oceanic Technol.*, *18*, 1735–1746, doi:10.1175/1520-0426(2001)018<1735:CMPITS>2.0.CO;2.

Elgar, S., B. Raubenheimer, and R. T. Guza (2005), Quality control of acoustic Doppler velocimeter data in the surfzone, *Meas. Sci. Technol.*, *16*, 1889–1893, doi:10.1088/0957-0233/16/10/002.

Emery, W. J., and R. E. Thomson (2001), *Data Analysis Methods in Physical Oceanography*, 2nd ed., Elsevier Sci., Amsterdam.
Feddersen, F. (2004), Effect of wave directional spread on the radiation stress: Comparing theory and observations, *Coastal Eng.*, *51*, 473–481, doi:10.1016/j.coastaleng.2004.05.008.
Feddersen, F., R. T. Guza, and S. Elgar (2004), Inverse modeling of one-dimensional setup and alongshore current in the nearshore, *J. Phys. Oceanogr.*, *34*, 920–933, doi:10.1175/1520-0485(2004)034<0920:IMOOSA>2.0.CO;2.
Fortunato, A. B., A. Oliveira, and A. M. Baptista (1999), On the effect of tidal flats on the hydrodynamics of the Tagus estuary, *Oceanol. Acta*, *22*, 31–44, doi:10.1016/S0399-1784(99)80030-9.
Friedrichs, C. T., and O. S. Madsen (1992), Nonlinear diffusion of the tidal signal in frictionally dominated embayments, *J. Geophys. Res.*, *97*, 5637–5650, doi:10.1029/92JC00354.
Geyer, W. R. (1997), Influence of wind on dynamics and flushing of shallow estuaries, *Estuarine Coastal Shelf Sci.*, *44*, 713–722, doi:10.1006/ecss.1996.0140.
Geyer, W. R., J. H. Trowbridge, and M. M. Bowden (2000), The dynamics of a partially mixed estuary, *J. Phys. Oceanogr.*, *30*, 2035–2048, doi:10.1175/1520-0485(2000)030<2035:TDOAPM>2.0.CO;2.
Grant, W. D., and O. S. Madsen (1979), Combined wave and current interaction with a rough bottom, *J. Geophys. Res.*, *84*(C4), 1797–1808, doi:10.1029/JC084iC04p01797.
Hench, J. L., and R. A. Luettich (2003), Transient tidal circulation and momentum balances at a shallow inlet, *J. Phys. Oceanogr.*, *33*, 913–932, doi:10.1175/1520-0485(2003)33<913:TTCAMB>2.0.CO;2.
Hench, J. L., B. O. Blanton, and R. A. Luettich (2002), Lateral dynamic analysis and classification of barotropic tidal inlets, *Cont. Shelf Res.*, *22*, 2615–2631, doi:10.1016/S0278-4343(02)00117-6.
Herbers, T. H. C., and R. T. Guza (1990), Estimation of directional wave spectra from multi-component observations, *J. Phys. Oceanogr.*, *20*, 1703–1724, doi:10.1175/1520-0485(1990)<1703:EODWSF>2.0.CO;2.
Jay, D. A. (1991), Green's law revisited: Tidal long-wave propagation in channels with strong topography, *J. Geophys. Res.*, *96*, 20,585–20,598, doi:10.1029/91JC01633.
Jessup, A., R. A. Holman, C. Chickadel, S. Elgar, G. Farquharson, M. C. Haller, A. L. Kurapov, H. T. Özkan- Haller, B. Raubenheimer, and J. M. Thomson (2012), Data assimilation and remote sensing for littoral applications, Abstract OS14A-01 presented at 2012 Fall Meeting, AGU, San Francisco, Calif., 3–7 Dec.
Kang, K., and D. Di Iorio (2006), Depth- and current-induced effects on wave propagation into the Altamaha River Estuary, Georgia, *Estuarine Coastal Shelf Sci.*, *66*(3–4), 395–408, doi:10.1016/j.ecss.2005.09.008.
Kraus, E. (1972), *Atmosphere-Ocean Interaction*, Oxford Univ. Press, London, 275 pp.
Kuik, A. J., G. Ph. van Vledder, and L. H. Holthuijsen (1988), A method for the routine analysis of pitch-and-roll buoy wave data, *J. Phys. Oceanogr.*, *18*, 1020–1034, doi:10.1175/1520-0485(1988)018<1020:AMFTRA>2.0.CO;2.
Large, W., and S. Pond (1981), Open ocean momentum flux measurements in moderate to strong winds, *J. Phys. Oceanogr.*, *11*, 324–336, doi:10.1175/1520-0485(1981)011<0324:OOMFMI>2.0.CO;2.
Lentz, S., R. T. Guza, S. Elgar, F. Feddersen, and T. H. C. Herbers (1999), Momentum balances on the North Carolina inner shelf, *J. Geophys. Res.*, *104*, 18,205–18,226, doi:10.1029/1999JC900101.
Li, C. (2013), Subtidal water flux through a multiple-inlet system: Observations before and during a cold front event and numerical experiments, *J. Geophys. Res.*, *118*, 1877–1892, doi:10.1002/jgrc.20149.
Li, C., and J. O'Donnell (2005), The effect of channel length on the residual circulation in tidally dominated channels, *J. Phys. Oceanogr.*, *35*, 1826–1840, doi:10.1175/JPO2804.1.
Lippmann, T. C., J. D. Irish, and J. Hunt (2013), Subtidal flow structure in tidally modulated inlets, in *Proceedings of Coastal Dynamics 2013*, edited by P. Bonneton and T. Garlan, pp. 1095–1104, SHOM (http://www.shom.fr/), Arcachon, France.
Longuet-Higgins, M. S., and R. W. Stewart (1964), Radiation stresses in water waves; a physical discussion, with applications, *Deep Sea Res. Oceanogr. Abstr.*, *11*, 529–562, doi:10.1016/0011-7471(64)90001-4.
MacMahan, J., J. van de Kreeke, A. Reniers, S. Elgar, B. Raubenheimer, E. Thornton, M. Weltmer, P. Rynne, and J. Brown (2014), Fortnightly tides and subtidal motions in a choked inlet, *Estuarine Coastal Shelf Sci*, doi:10.1016/j.ecss.2014.03.025, in press.
Malhadas, M. S., P. C. Leitão, A. Silva, and R. Neves (2009), Effect of coastal waves on sea level in Óbidos Lagoon, Portugal, *Cont. Shelf Res.*, *29*, 1240–1250, doi:10.1016/j.csr.2009.02.007.
Olabarrieta, M., R. Medina, and S. Castanedo (2010), Effects of wave–current interaction on the current profile, *Coastal Eng.*, *57*(7), 643–655, doi:10.1016/j.coastaleng.2010.02.003.
Olabarrieta, M., J. C. Warner, and N. Kumar (2011), Wave-current interaction in Willapa Bay, *J. Geophys. Res.*, *116*, C12014, doi:10.1029/2011JC007387.
Pacheco, A., Ó. Ferreira, J. J. Williams, E. Garel, A. Vila-Concejo, and J. A. Dias (2010), Hydrodynamics and equilibrium of a multiple-inlet system, *Mar. Geol.*, *274*, 32–42, doi:10.1016/j.margeo.2010.03.003.
Peña, A., and S.-E. Gryning (2008), Charnock's roughness length model and non-dimensional wind profiles over the sea, *Boundary Layer Meteorol.*, *128*, 191–203, doi:10.1007/s10546-008-9285-y.
Piedracoba, S., C. Souto, M. Gilcoto, and P. C. Pardo (2005), Hydrography and dynamics of the Ría de Ribadeo (NW Spain), a wave driven estuary, *Estuarine Coastal Shelf Sci.*, *65*, 726–738, doi:10.1016/j.ecss.2005.07.013.
Rabiner, L., and B. Gold (1975), *Theory and Application of Digital Signal Processing*, Prentice-Hall, Englewood Cliffs, N. J.
Raubenheimer, B., S. Elgar, and R. T. Guza (1998), Estimating wave heights from pressure measured in sand bed, *J. Waterw. Port Coastal Ocean Eng.*, 151–154, doi:10.1061/(ASCE)0733-950X(1998)124:3(151).
Raubenheimer, B., R. T. Guza, and S. Elgar (2001), Field observations of wave-driven setdown and setup, *J. Geophys. Res.*, *106*, 4629–4638, doi:10.1029/2000JC000572.
Riggs, S. R., W. J. Cleary, and S. W. Snyder (1995), Influence of inherited geologic framework on barrier shoreface morphology and dynamics, *Mar. Geol.*, *126*, 213–234, doi:10.1016/0025-3227(95)00079-E.
Salles, P. (2001), Hydrodynamic controls on multiple tidal inlet persistence, PhD dissertation, Mass. Inst. of Technol. and Woods Hole Oceanogr. Inst., Mass., 272 pp.
Salles, P., G. Voulgaris, and D. G. Aubrey (2005), Contribution of nonlinear mechanisms in the persistence of multiple tidal inlet systems, *Estuarine Coastal Shelf Sci.*, *65*, 475–491, doi:10.1016/j.ecss.2005.06.018.
Sempreviva, A. M., S. E. Larsen, N. G. Mortensen, and I. Troen (1990), Response of neutral boundary layers to changes of roughness, *Boundary Layer Meteorol.*, *50*, 205–225, doi:10.1007/2FBF00120525.
Signell, R. P., and W. R. Geyer (1991), Transient eddy formation around headlands, *J. Geophys. Res.*, *96*, 2561–2575, doi:10.1029/90JC02029.

Smith, J. M. (2002), Wave pressure gauge analysis with current, *J. Waterw. Port Coastal Ocean Eng.*, *128*, 271–275, doi:10.1061/(ASCE)0733-950X(2002)128:6(271).

Smith, N. P. (1993), Tidal and nontidal flushing of Florida's Indian River Lagoon, *Estuaries*, *16*, 739–746, doi:10.2307/1352432.

Smith, S. D. (1980), Wind stress and heat flux over the ocean in gale force winds, *J. Phys. Oceanogr.*, *10*, 709–726, doi:10.1175/1520-0485(1980)010<0709:WSAHFO>2.0.CO;2.

Speer, P. E., and D. G. Aubrey (1985), A study of non-linear tidal propagation in shallow inlet/estuarine systems part II: theory, *Estuarine Coastal Shelf Sci.*, *21*, 207–224, doi:10.1016/0272-7714(85)90097-6.

Stommel, H. and H. G. Farmer (1952), On the nature of estuarine circulation, *Ref*. 52–88, Woods Hole Oceanogr. Inst., Woods Hole, Mass.

Swenson, E. M., and W. S. Chuang (1983), Tidal and subtidal water volume exchange in an estuarine system, *Estuarine Coastal Shelf Sci.*, *16*, 229–240, doi:10.1016/0272-7714(83)90142-7.

Tutak, B., and Y. P. Sheng (2011), Effect of tropical cyclones on residual circulation and momentum balance in a subtropical estuary and inlet: Observation and simulation, *J. Geophys. Res.*, *116*, C06014, doi:10.1029/2011JC006988.

Wargula, A., B. Raubenheimer, and S. Elgar (2013), The effects of wave forcing on circulation at New River Inlet, NC, in *Proceedings of Coastal Dynamics 2013*, edited by P. Bonneton and T. Garlan, pp. 1871–1880, SHOM (http://www.shom.fr/), Arcachon, France.

Waterhouse, A. F., and A. Valle-Levinson (2010), Transverse structure of subtidal flow in a weakly stratified subtropical tidal inlet, *Cont. Shelf Res.*, *30*, 281–292, doi:10.1016/j.csr.2009.11.008.

Winant, C. D. (2008), Three-dimensional residual tidal circulation in an elongated, rotating basin, *J. Phys. Oceanogr.*, *38*, 1278–1295, doi:10.1175/2007JPO3819.1.

Wong, K.-C., and A. Valle-Levinson (2002), On the relative importance of the remote and local wind effects on the subtidal exchange at the entrance to the Chesapeake Bay, *J. Mar. Res.*, *60*(3), 477–498, doi:10.1357/002224002762231188.

Wong, K.-C., and J. E. Moses-Hall (1998), On the relative importance of the remote and local wind effects to the subtidal variability in a coastal plain estuary, *J. Geophys. Res.*, *103*(C9), 18,393–18,404, doi:10.1029/98JC01476.

Zippel, S., and J. M. Thomson (2012), Wave Breaking at New River Inlet, Abstract OS11G-03 presented at 2012 Fall Meeting, AGU, San Francisco, Calif., 3–7 Dec.